Turbulent Hybrid Bearings With Fluid Inertia Effects

Luis San Andrés
Research Associate,
Mechanical Engineering Department,
Texas A&M University,
College Station, Texas 77843
Mem. ASME

High speed hybrid bearings for cryogenic applications demand large levels of external pressurization to provide substantial load capacity. These conditions give rise to large film Reynolds numbers, and thus, cause the fluid flow within the bearing film to be turbulent and dominated by fluid inertia effects both at the recess edges and at the thin film lands. The analysis includes the effect of recess fluid compressibility and a model for the pressure rise within the recess region. Flow turbulence is simulated by friction factors dependent on the local Reynolds numbers and surface conditions. A perturbation method is used to calculate the zeroth and first flow fields and determine the bearing steady-state and dynamic force response. Comparison of results with existing experimental data shows the accuracy of the present full inertial-turbulent analysis. A roughened bearing surface is shown to improve considerably the stability characteristics of hybrid bearings operating at high speeds.

Introduction

Hydrostatic and hybrid (combined hydrostatic and hydrodynamic) journal bearings (HJBs) are the subject of increased attention because of their potential application as support elements in cryogenic high speed turbomachinery. These bearings have been proposed for primary and auxiliary space-power applications due to their long lifetime, low friction and wear, and good dynamic force response characteristics. Despite these attractive features, there is yet further research needed, both analytical as well as experimental, to consider the extension of these bearings into high speed applications.

Analyses of turbulent hybrid bearings have to date been based on the numerical solution to the modified turbulent flow Reynolds equation with fluid inertia accounted locally at the recess edges by simple Bernoulli type relationships. The published contributions on the subject are numerous, and only the references relevant to the present work are briefly discussed.

Redecliff and Vohr (1969) introduced a FD model for turbulent flow HJBs. The analysis shows that fluid inertia gives rise to lower flow rates if compared to an inertialess solution, but it does not affect the bearing load capacity. Redecliff and Vohr tested a LO2 and a LH2 bearing to be used in rocket turbopumps. Experimental data for both test programs agreed well with steady-state predictions. Discrepancies were observed in the measured flow rates which were lower than the predicted values.

Heller (1974) presented a similar numerical solution which included the local effect of fluid inertia at the recess edges. A six pocket hybrid bearing was tested with water. Experiments showed that fluid inertia considerably affected flow rates in comparison to predictions not including this effect. Deguerce and Nicholas (1975) presented predictions which compared well with Heller's measurements although the analysis neglected fluid inertia edge effects. Guidez et al. (1981) developed an analysis for sodium hybrid bearings. Measured pressures for a water HJB showed that inertia effects substantially exceeded the predicted values.

Artiles, Walowit, and Shapiro (1982) presented a well documented numerical method for prediction of the static and dynamic force performance of turbulent HJBs. The analysis includes the local effect of fluid inertia at the recess edges, but *the fluid compressibility effect at the recess volumes is neglected*. Turbulent shear factors, based on the theory of Elrod and Ng (1967), are calculated separately for pressure (Poiseuille) and shear (Couette) dominated turbulent flows. Artiles et al. predictions show that fluid inertia effects are important for the cryogenic sample bearings presented. The results also indicate large bearing power losses for high Reynolds numbers flows.

Ho and Chen (1980, 1984) and Lingard and Chen (1982) presented experimental data for HJBs with pockets of non-uniform depth. At low supply pressures, fluid pressure is observed to be uniform within the recess region. However, for large external pressures, a pressure peak appears at the location of the capillary restrictor. The influence of rotation on the recess pressures is shown to generate a pressure rise at the downstream section of the recess. The hydrodynamic effect on the load capacity is very pronounced at low supply pressures with attitude angles larger than 90 deg due to fluid inertia effects.

Chaomleffel and Nicholas (1986) presented measurements for a 3-recess, water lubricated HJB. For hybrid operation at large eccentricities, a substantial pressure generation on the bearing lands occurred due to enhanced hydrodynamic effects.

Contributed by the Tribology Division of THE AMERICAN SOCIETY OF MECHANICAL ENGINEERS and presented at the Joint ASME/STLE Tribology Conference, Toronto, Canada, October 7–10. Manuscript received by the Tribology Division October 19, 1989; revised manuscript received May 13, 1990. Paper No. 90-Trib-3. Associate Editor: D. C. Sun.

A pressure drop was observed only on the edge downstream of the supply line. The magnitude of the measured edge pressure drop appears to be dependent on the journal speed and the recess depth. Comparisons of the experimental values with predictions based on solution of the turbulent Reynolds equation are also included. The numerical calculations for load and flow rate are consistently larger than the measurements, and predicted edge pressure drops are smaller than those observed. Recently, Bou-Said and Chaomleffel (1988) have also presented numerical comparisons with the experimental results of Chaomleffel et al. These updated predictions show the same differences, although improved load correlations are obtained.

Measurements of rotordynamic coefficients for turbulent HJBs have been presented by Murphy and Wagner (1986). Test data were compared with predictions based on the analysis of Artiles et al. (1982). The experimental measurements show that direct stiffnesses are about 20 percent lower than predictions, while direct damping coefficients are roughly equal. Measured cross-coupled stiffnesses are less than predicted and actually shown to be a stabilizing factor in the bearing dynamic performance.

Fluid inertia on the film lands of laminar flow, capillary restricted HJBs has been considered approximately by Ghosh (1989). Numerical predictions present an optimum equivalent dynamic stiffness at a given excitation frequency. Below this frequency, compressibility effects are important; while above this value, fluid inertia is dominant and eventually leads to null or negative dynamic stiffness.

High speed hybrid bearings operating with low viscosity cryogenic fluids require large levels of external pressurization to provide substantial load capacity. These unique conditions give rise to large film Reynolds numbers, and thus, cause the flow within the bearing film to be highly turbulent and dominated by fluid inertia effects both at the recess edges and in the thin film land regions. A survey of operating conditions for current HJBs handling cryogenic fluids shows that typical film Reynolds numbers based on pressure flow (Rep) range from 1×10^4 to 1×10^6, while Reynolds numbers based on rotational speed (Re) could reach values as high as 1×10^5. These large values of the Reynolds numbers indicate that fluid inertia is a major factor in HJB performance. Existing analytical treatments confined within the realm of classical turbulent lubrication theory can not interpret accurately the actual complex phenomena occurring in HJBs. Therefore, an improved analysis is required to assess quantitatively the magnitude of fluid inertia effects on the static and dynamic force response of turbulent HJBs.

Analysis

The geometry of a multirecess hybrid bearing is schematically shown in Fig. 1. Fluid enters the bearing across a restrictor orifice, passes through a recess area of relatively large clearance, flows into the film lands and then exits the bearing. For hydrostatic operation, the recess pressure is regarded as uniform on the recess volume, while at the recess boundary a pressure drop due to fluid inertia occurs on the sudden transition from the deep recess into the film land region. Experimental evidence shows that for hybrid operation a pressure rise exists on the downstream region of the restrictor supply line as sketched in Fig. 2.

The performance characteristics of the bearing are governed by momentum and continuity considerations in the fluid film lands as well as continuity of flow through the bearing recesses. The former defines the pressure and velocity fields over the

Nomenclature

b = recess circumferential length [m]
c = radial clearance [m]
$C_{XX}, C_{XY}, C_{YX}, C_{YY}$ = damping coefficients [Ns/m]
C_d = orifice discharge coefficient
D = 2.R bearing diameter [m]
d_0 = orifice diameter [m]
f_J, f_B = turbulent friction factors at journal and bearing surfaces

$$f_J = 0.001375\left[1+\left(10^4\frac{r_J}{H}+\frac{5\times10^5}{R_J}\right)^{1/2.65}\right]$$

$$f_B = 0.001375\left[1+\left(10^4\frac{r_B}{H}+\frac{5\times10^5}{R_B}\right)^{1/2.65}\right]$$

F_x, F_y = fluid film forces in X and Y directions [N]
$h = H/c = 1 + \epsilon_x \cos\theta + \epsilon_y \sin\theta$ dimensionless film thickness
h_x, h_y = $\cos\theta$, $\sin\theta$
H_r = recess depth [m]
$K_{XX}, K_{XY}, K_{YX}, K_{YY}$ = stiffness coefficients [N/m]
k_x, k_y = $(1/2)(k_J + k_B)$ dimensionless shear parameters in circumferential and axial directions
k_J, k_B = $f_J R_J, f_B R_B$ turbulent shear parameters at journal and bearing surfaces
k_r = Re$_r$ .681/7.753 turbulent shear flow factor at recess
k_c = 0.25 $[u_0 k_{J0} - (u_0 - \Lambda)k_{B0}]$ turbulent Couette shear stress factor at rotor surface
L, 1 = bearing axial width, recess axial width [m]
N_{rec} = number of recesses on bearing
$M_{XX}, M_{XY}, M_{YX}, M_{YY}$ = inertia or added mass coefficients [Kg]
P = fluid pressure [N/m^2]
P_s, P_a, P_r, P_e = external supply and discharge pressures, recess and edge pressures [N/m^2]
$p = (P - P_a)/(P_s - P_a)$ dimensionless pressure
p_x, p_y = dimensionless dynamic pressures
$q_r = \int h(\mathbf{v} \cdot \mathbf{n})\, d\Gamma r = Q_r \cdot \mu/c^3(P_s - P_a)$ dimensionless recess flow rate
Re = $\rho\Omega cR/\mu$ nominal circumferential flow Reynolds number
Re$_H$ = $\rho\Omega HR/\mu$ film Reynolds number due to rotation
Re$_p$ = $\rho c^3(P_s - P_a)/(\mu^2 R)$ pressure flow Reynolds number
Re$_p^*$ = Re$_p \cdot c/R$ modified pressure flow Reynolds number
Re$_r$ = $\rho\Omega(H_r + c)R/\mu$ rotation film Reynolds number at recess
Re$_s$ = $\rho\omega c^2/\mu$ squeeze film Reynolds number

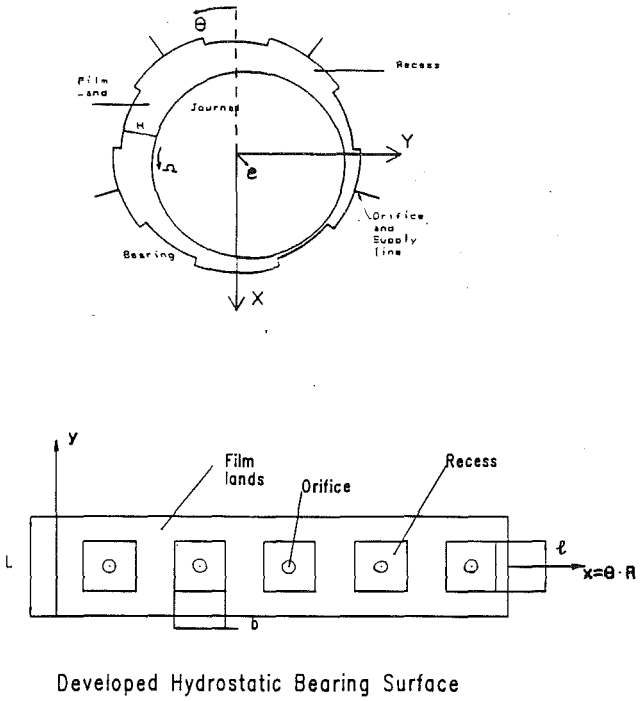

Fig. 1 Geometry of a hydrostatic journal bearing (HJB). (*a*) description of coordinate systems, (*b*) developed bearing surface for analysis.

bearing film lands, whereas the latter provides values for the pressure in the recesses.

For an isoviscous incompressible fluid, the continuity and momentum equations for the turbulent bulk flow on the film lands are given by Launder and Leschziner (1978) as:

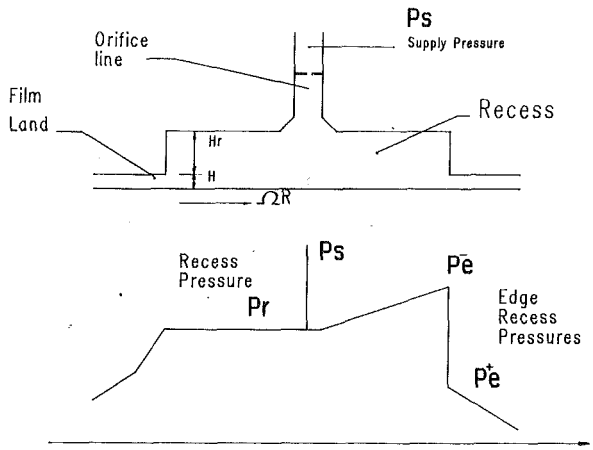

Fig. 2 Conceptual description of pressure rise and pressure drop at recess edges

$$\frac{\partial}{\partial x}(UH)+\frac{\partial}{\partial y}(VH)+\frac{\partial H}{\partial t}=0 \tag{1}$$

$$-H\frac{\partial P}{\partial x}=\frac{\mu}{H}\left(k_x U-k_J\frac{R\Omega}{2}\right)+\rho\left\{\frac{\partial}{\partial t}(HU)+\frac{\partial}{\partial x}(HU^2)+\frac{\partial}{\partial y}(HUV)\right\} \tag{2}$$

Nomenclature (cont.)

R_J, R_B = $(\rho/\mu)H[(U-\Omega R)^2+V^2]^{1/2}$; $(\rho/\mu)H[U^2+V^2]^{1/2}$ Reynolds numbers relative to journal and bearing surfaces
r_J, r_B = surface roughness at journal and bearing [m]
T_0 = fluid film resistance torque [Nm]
U, V = fluid mean flow velocities in circumferential and axial directions [m/s]
u, v = $(U, V)\mu R/c^2(P_s-P_a)$ dimensionless mean flow velocities
V_r, V_s = $(H_r+H)\,lb+V_s$ total recess and orifice supply volumes [m^3]
$\{X, Y\}$ = inertial coordinate system
α_r = $k_r\,(b/D)\eta^2$ recess pressure dimensionless shear coefficient
α_x = $\dfrac{\mathrm{Re}_p^*\,(1+\xi_x)\,(1-\eta^2)}{\left(1+\dfrac{1.95}{\mathrm{Re}_H^{.43}}\right)}$ recess pressure circumferential entrance loss coefficient
α_y = $(1+\xi_y)\,(1-\eta^2)\mathrm{Re}_p^*$ recess pressure axial entrance loss coeff
ξ_x, ξ_y = empirical entrance loss coefficients in circumferential and axial directions
β = $(1/\rho)\,(\partial\rho/\partial P)$ fluid compressibility factor [m^2/N]
δ = $C_d(\pi/4)d_0^2\mu\sqrt{2}/[c^3\sqrt{\rho(P_s-P_a)}]$ dimensionless orifice parameter
λ_1 = $\mu\omega lb/[c^2(P_s-P_a)$ recess frequency parameter
λ_2 = $V_r\beta(P_s-P_a)/[clb]$ compressibility parameter
Λ = $\mu\Omega R^2/[c^2(P_s-P_a)]$ rotational speed parameter
σ = $\mu\omega R^2/[c^2(P_s-P_a)]$ frequency parameter at film lands
ω = excitation or whirling frequency [1/s]
Ω = rotational speed of journal [1/s]
ϵ_x, ϵ_y = e_x/c, e_y/c dimensionless journal eccentricities in X and Y direction
$\Delta\epsilon_x, \Delta\epsilon_y$ = dimensionless perturbed eccentricities
τ = ωt dimensionless time coordinate
θ, ξ = x/R, y/R dimensionless circumferential and axial coordinates
$\gamma_{uu}, \gamma_{uv}, \gamma_{vu}, \gamma_{vv}, \gamma_{u0}, \gamma_{v0}$ = first-order turbulent shear coefficients (Appendix A)
η = $H/(H_r+H)$ ratio of land film thickness to recess depth
Γ_r = recess boundary

Subscripts

0 = refers to zeroth order solution
r, e = refers to bearing recesses and recess edge
α = refers to first-order solution

$$-H\frac{\partial P}{\partial y} = \frac{\mu}{H}k_y V + \rho\left\{\frac{\partial}{\partial t}(HV) + \frac{\partial}{\partial x}(HUV) + \frac{\partial}{\partial y}(HV^2)\right\} \quad (3)$$

The turbulent shear parameters k_x and k_y are taken as local functions of the friction factors f_J and f_B relative to the journal and bearing surfaces (Hirs, 1973; Nelson, 1987). The present turbulence model has been selected solely on grounds of simplicity, ability to represent surface roughness, and accuracy to model simple turbulent flows.

The pressure and velocity fields are continuous in the circumferential direction. At the bearing exit plane, the pressure takes a constant value equal to the ambient or sump pressure (P_a). At the interface with the recess boundary, the velocity vector relative to the rotating journal is considered to be normal to the recess edges (Artiles et al., 1982).

The continuity equation at the recess is defined by the global balance between the flow through the orifice restrictor, the recess outflow into the film lands (Q_r) and the temporal change of fluid mass within the recess volume. The recess flow continuity equation is expressed as:

$$C_d\frac{\pi d_0^2}{4}\left[\frac{2(P_s-P_r)}{\rho}\right]^{1/2} = Q_r + \frac{\partial V_r}{\partial t} + V_r\beta\frac{\partial P_r}{\partial t} \quad (4)$$

It has been noted that for hybrid operation, a pressure rise occurs within the downstream portion of the recess. In the analysis, this region is considered as a one-dimensional step bearing and the pressure *just* before the recess edge is obtained from the following relationship (Constantinescu and Galetuse, 1975):

$$P_e^- = P_r - \mu\, k_r\frac{\eta^2}{c^2}\left(U\eta - \frac{\Omega R}{2}\right)\cdot\frac{b}{2} \quad (5)$$

The local acceleration of fluid from relatively stagnant conditions at the recess to a high velocity at the film lands causes a sudden pressure drop at the recess boundary. The pressure at the entrance to the film lands is modeled by simple Bernoulli relationships based on the model developed by Constantinescu et al. (1975), and given for the circumferential and axial directions as:

$$P_e^+ = P_e^- - (\rho/2)\left(1+\frac{1.95}{\mathrm{Re}_H^{.43}}\right)(1+\xi_x)(1-\eta^2)U^2,\ U\cdot\mathbf{n}>0$$
$$P_e^+ = P_r - (\rho/2)(1+\xi_y)(1-\eta^2)V^2,\ V>0 \quad (6)$$

The coefficients introduced in equations (5) and (6) refer to turbulent flow only. For laminar flows, equivalent expressions are used according to Constantinescu and Galetuse (1975).

Perturbation Analysis and Dimensionless Equations. For steady-state conditions, the journal center is at the equilibrium position (e_{x0}, e_{y0}). Superimposed on this position, the journal center describes small amplitude motions Δe_x and Δe_y at frequency ω. The dimensionless film thickness is described by the real part of the following expression:

$$h = h_0 + e^{i\tau}(\Delta\epsilon_x\cos\theta + \Delta\epsilon_y\sin\theta) \quad (7)$$
$$h_0 = 1 + \epsilon_{x0}\cos\theta + \epsilon_{y0}\sin\theta;\ \tau=\omega t;\ i=\sqrt{-1}$$

For small amplitude motions, the dimensionless velocity and pressure fields, as well as the shear coefficients (k_x, k_y), are expressed as the sum of a zeroth order field and first-order complex fields, describing the equilibrium condition and the perturbed dynamic motion, respectively. Hence

$$p = p_0 + e^{i\tau}(\Delta\epsilon_x p_x + \Delta\epsilon_y p_y)$$
$$u = u_0 + e^{i\tau}(\Delta\epsilon_x u_x + \Delta\epsilon_y u_y)$$
$$v = v_0 + e^{i\tau}(\Delta\epsilon_x v_x + \Delta\epsilon_y v_y)$$
$$k_x = k_{x0} + e^{i\tau}(\Delta\epsilon_x k_{xx} + \Delta\epsilon_y k_{xy})$$
$$k_y = k_{y0} + e^{i\tau}(\Delta\epsilon_x k_{yx} + \Delta\epsilon_y k_{yy}) \quad (8)$$

Substitution of the flow variables as given above into the governing equations (1) to (6) yields the following differential equations for the zeroth and first-order flow fields.

Zeroth-order dimensionless equations:

(a) on film lands

$$\frac{\partial}{\partial\theta}(u_0h_0) + \frac{\partial}{\partial\xi}(v_0h_0) = 0 \quad (9)$$

$$-h_0\frac{\partial p_0}{\partial\theta} = \frac{1}{h_0}\left(k_{x0}u_0 - k_{J0}\frac{\Lambda}{2}\right) + \mathrm{Re}_p^*\left\{\frac{\partial}{\partial\theta}(h_0u_0^2) + \frac{\partial}{\partial\xi}(h_0u_0v_0)\right\} \quad (10)$$

$$-h_0\frac{\partial p_0}{\partial\xi} = \frac{1}{h_0}k_{y0}v_0 + \mathrm{Re}_p^*\left\{\frac{\partial}{\partial\theta}(h_0u_0v_0) + \frac{\partial}{\partial\xi}(h_0v_0^2)\right\} \quad (11)$$

(b) For each recess, the flow through the orifice equals the inlet flow to the bearing lands,

$$\delta(1-p_{r0})^{1/2} = q_{r0} = \int_{\Gamma_r} h_0(\mathbf{v}_0\cdot\mathbf{n})\,d\Gamma, \quad (12)$$

For hybrid operation, the circumferential edge pressure rise is given by

$$p_{e0}^- = p_{r0} - \alpha_r\left[u_0\eta - \frac{\Lambda}{2}\right] \quad (13)$$

The edge pressures at the entrance to the film region are related to the recess pressure and inlet film velocity by:

$$p_{e0}^+ = p_{e0}^- - \alpha_x u_0^2/2;\ u_0\cdot\mathbf{n}>0$$
$$p_{e0}^+ = p_{r0} - \alpha_y v_0^2/2;\ v_0>0 \quad (14)$$

First-order dimensionless equations:

(a) On film lands:

$$\frac{\partial}{\partial\theta}(u_\alpha h_0 + u_0h_\alpha) + \frac{\partial}{\partial\xi}(v_\alpha h_0 + v_0h_\alpha) = -i\,\sigma\,h_\alpha \quad (15)$$

$$-h_0\frac{\partial p_\alpha}{\partial\theta} = (\gamma_{uu} + i\,\mathrm{Re}_s h_0)u_\alpha + \gamma_{uv}v_\alpha + \gamma_{u0}h_\alpha + \mathrm{Re}_p^*\left\{\frac{\partial}{\partial\theta}(u_0h_0u_\alpha) + \frac{\partial}{\partial\xi}(v_0h_0u_\alpha) + h_0u_\alpha\frac{\partial u_0}{\partial\theta} + h_0v_\alpha\frac{\partial u_0}{\partial\xi}\right\} \quad (16)$$

$$-h_0\frac{\partial p_\alpha}{\partial\xi} = (\gamma_{vv} + i\,\mathrm{Re}_s h_0)v_\alpha + \gamma_{vu}u_\alpha + \gamma_{v0}h_\alpha + \mathrm{Re}_p^*\left\{\frac{\partial}{\partial\theta}(u_0h_0v_\alpha) + \frac{\partial}{\partial\xi}(v_0h_0v_\alpha) + h_0u_\alpha\frac{\partial v_0}{\partial\theta} + h_0v_\alpha\frac{\partial v_0}{\partial\xi}\right\} \quad (17)$$

where the subscript $\alpha = X$ or Y denotes perturbation in the inertial X and Y directions, and $h_x = \cos\theta$ and $h_y = \sin\theta$, respectively. The coefficients γ_{uu}, γ_{vu}, etc., arise from the perturbation of the shear stress factors k_x, k_y, and k_J, and their explicit formulas are given in detail in Appendix A.

(b) On each recess the continuity equation takes the linearized form:

$$-p_{r\alpha}\left[\frac{\delta^2}{2q_{r0}} + i\lambda_1\lambda_2\right] = i\lambda_1 h_{r\alpha} + \int_{\Gamma_r}[h_\alpha\mathbf{v}_0 + h_0\mathbf{v}_\alpha]\cdot\mathbf{n}\,d\Gamma_r, \quad (18)$$

and the first-order edge pressures are given by:

$$p_{e\alpha}^+ = p_{r\alpha} - \alpha_x u_0u_\alpha;\ u_0\cdot\mathbf{n}>0$$
$$p_{e\alpha}^+ = p_{r\alpha} - \alpha_y v_0v_\alpha;\ v_0>0 \quad (19)$$

Table 1 Description of 3 recess hydrostatic water bearing studied experimentally by Chaomleffel and Nicholas (1986). Bearing geometry and operating conditions.

3 Recess Hydrostatic Water Bearing from Chaomleffel and Nicholas (1986)

Geometry:
Diameter = 80mm(3.15 in)
Length = 80 mm(3.15 in)
Recess lxb = 50mm x 62.83mm

Clearance = 0.125mm(0.005in)

Recess depth Hr = 2mm(0.078 in)

Orifice diameter = 4.1mm

Fluid: Water at 20C,
Viscosity, 0.001 Pa sec
Density: 1000 Kg/m3

Pressure Supply: 0.4MPa(58psi)

Journal speed: 0 to 9000 rpm

Dimensionless Parameters

Reynolds Numbers: Rep=18773, Re$_p$=58.66
Speed Parameter : 0 to 0.246
Rotation Reynolds Number: 0 to 4618

L/D=1, l/L=.625, N b/πD=.75
c/R=0.0031, Hr/c=16

Fluid Film Forces and Dynamic Force Coefficients. Once a solution for the zeroth and first-order flow fields is determined, fluid film forces are calculated by integration of the pressure field on the journal surface. The perturbation analysis allows the steady-state forces and dynamic force coefficients to be obtained from the equations:

$$F\alpha_0 = 2(P_s - P_a)R^2 \int_0^{L/D} \int_0^{2\pi} p_0 h_\alpha d\theta \, d\xi \tag{20}$$

$$K_{\alpha\beta} - \omega^2 M_{\alpha\beta} + i\,\omega\, C_{\alpha\beta} = -2(P_s - P_a)\frac{R^2}{c} \int_0^{L/D} \int_0^{2\pi} p_\beta h_\alpha d\Theta \, d\xi \tag{21}$$

$$\alpha,\beta = x,y$$

The real part of the first-order pressure field gives rise to the dynamic stiffnesses, while its imaginary part renders the damping coefficients. The drag torque is given by integration of the wall shear stress at the journal surface,

$$T_0 = 2(P_s - P_a)R^2 c \int_0^{L/D} \int_0^{2\pi} \left[\frac{h_0}{2}\frac{\partial p_0}{\partial \theta} + \frac{k_c}{h_0}\right] d\theta \, d\xi \tag{22}$$

where k_c is the dimensionless Couette shear parameter at the journal surface as given by Hirs (1973).

The Numerical Solution Procedure. A finite difference scheme, based on the method of Launder and Leschziner (1978), has been implemented to solve the nonlinear PDEs governing the flow in the film lands. Discrete nonlinear difference equations are obtained by integration of the momentum and continuity equations over a typical fluid control volume. The velocities are determined at points which lie at interfaces midway between the nodes where the pressure is calculated. The scheme also implements the SIMPLE Consistent algorithm of Van Doormaal and Raithby (1984) to accelerate solution convergence. The iterative solution of the nonlinear equations in the film lands is coupled to a Newton-Raphson algorithm that estimates improved values of the recess pressures and satisfies the recess flow constraints.

Once the numerical solution to the zeroth order equations has been obtained, the first-order (perturbed) flow fields $\{u_\alpha, v_\alpha, p_\alpha\}$ can be calculated for a given frequency ω. The equations for the first-order solution are linear with coefficients fully determined by the zeroth-order solution. This enables a solution to the perturbed flow field to be found in the form of a component series.

On the numerical procedure implemented, fluid film cavitation is identified as local null pressures. This oversimplification is solely justified on grounds of its widespread usage. Fortunately it appears that, for the large supply pressures used in current cryogenic HJBs, cavitation is unlikely to occur except for operation at high eccentricities.

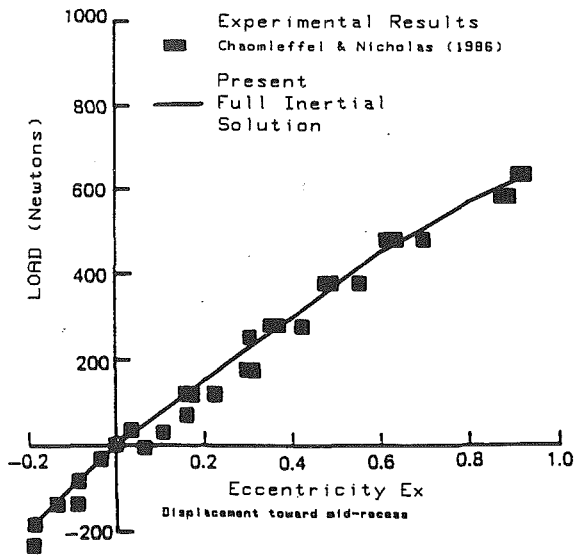

Fig. 3 Measured bearing load for hydrostatic operation. Experimental results of Chaomleffel and Nicholas (1986) and predictions from present full inertial analysis.

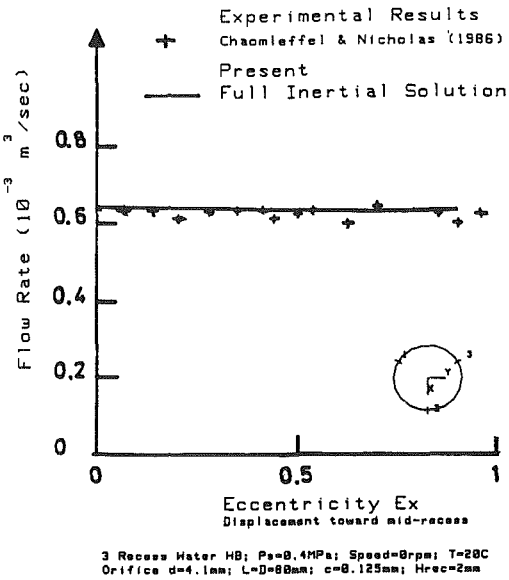

Fig. 4 Measured bearing flow rate for hydrostatic operation. Experimental results of Chaomleffel and Nicholas (1986) and predictions from present full inertial analysis.

For the concentric position, the numerical scheme presented is at its peak efficiency. Under this condition, the complete flow field needs to be calculated only for one recess due to symmetry. The flow in the other recesses is obtained by proper rotations.

The computer program developed has been implemented in a desktop micro computer and its speed of execution is relatively small. A typical mesh of 13 circumferential points by 9 axial points for *each* recess and adjacent land are selected for the analysis. Typical values of number of iterations for convergence of the zeroth order field are 4 to 5 on the recess pressures, and 20 to 40 on each solution for the flow field on the film lands. The first order solution takes about 10–15 iterations for each component field. The numerical scheme

converged successfully for all cases analyzed. No signs of numerical instability were present even in the cases in which orifice back flow occurred for high load conditions and large journal eccentricity operation.

Results and Discussion

Comparisons of Present Solution With Experimental Results. The present full inertial solution (FIS) has been correlated and validated with several experimental results available in the literature. Extensive comparisons both for exactness and performance have been conducted. Due to space considerations, the extent of the comparisons presented here is limited.

Chaomleffel and Nicholas (1986) presented experimental results for load, flow, and pressure for a 3-recess hydrostatic bearing. Table 1 shows the bearing description and operating conditions. Film pressures were measured at the bearing circumferential mid-plane by eleven pressure gauges located between 2 consecutive recesses. For hydrostatic operation, Figs. 3 and 4 show the measured bearing load capacity and flow rate for increasing values of the static journal eccentricity. For the range of eccentricity radii tested, the comparison between experimental values and the numerical results is excellent. Other numerical predictions from Chaomleffel and Nicholas (1986) and Bou-Said and Nicholas (1988), not included here for clarity, show consistently higher load capacities and lower flow rates for all eccentricities.

For the centered position, Fig. 5 shows a comparison of the measured pressures at the bearing circumferential mid-plane and the predictions of the FIS model. Results are presented for rotational speeds equal to 0, 5000, and 9000 rpm. For hybrid operation, the measured pressures at the downstream portion of the recess increase monotonically and at the recess edge and a large inertial pressure drop is observed. The experimental evidence suggest that the magnitude of the pressure rise and edge drop depend on the journal speed and the recess depth. The numerical predictions compare very well with the measurements. The error is not greater than 4 percent, except for the edge pressure drop at the highest speed which shows a greater measured magnitude. The experimental values are

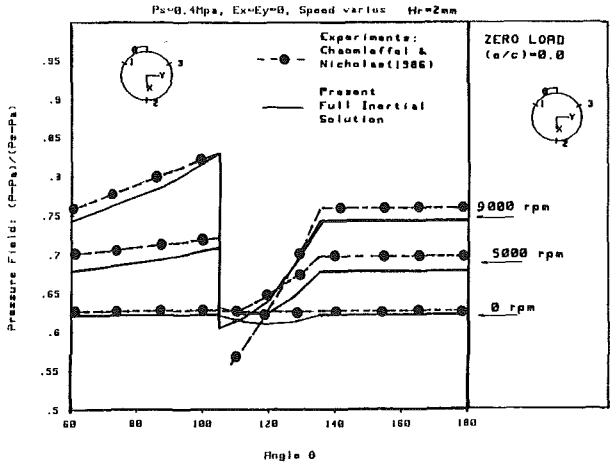

Fig. 5 Experimental pressure field for concentric operation. Measurements of Chaomleffel and Nicholas (1986) and comparison with predictions from present full inertial solution.

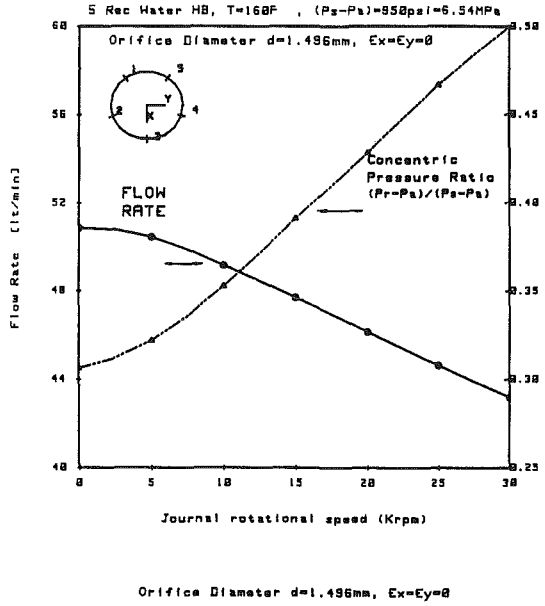

Fig. 7 Predicted flow rate and recess pressure ratio for test hydrostatic water bearing versus journal rotational speed. Concentric operation, Ps = 6.54 MPa, orifice diameter = 1.496 mm.

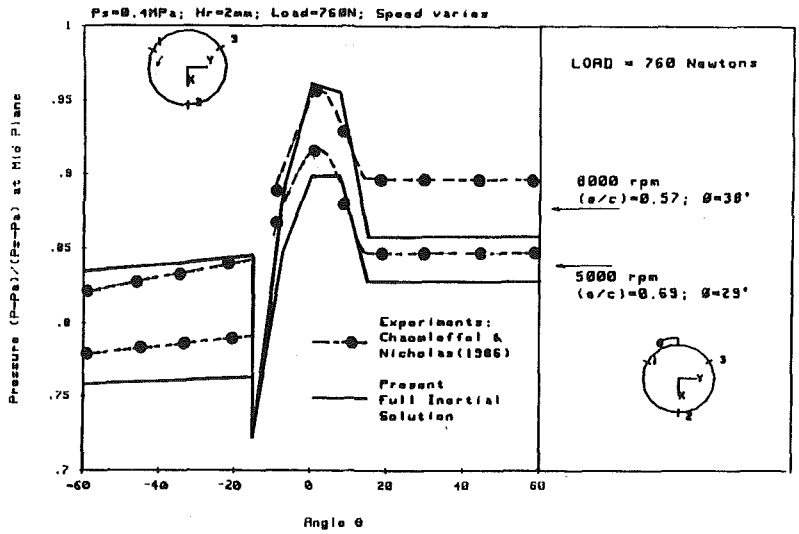

Fig. 6 Experimental pressure field for a load equal to 760 Newtons and speeds equal to 5000 and 8000 rpm. Measurements of Chaomleffel and Nicholas (1986) and comparison with predictions from present full inertial solution.

Table 2 Description of 5 recess hydrostatic water bearing under development for TAMU Hybrid Bearing Research program (1989). Bearing geometry and operating conditions.

5 Recess Hydrostatic Water Bearing
TAMU Experimental Program (1989)

Geometry:
Diameter = 76.2mm(3.00 in)
Length = 76.2mm(3.00 in)
Recess lxb = 27mm x 27mm

Clearance = 0.0762mm(0.003in)

Recess depth Hr = 0.457mm(0.018in)

Orifice diameter = 1.496mm

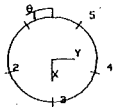

Fluid: Water at 71.1C(160F)
Viscosity, 3.98E-4 Pa·sec
Density: 977 Kg/m3

Pressure Supply:6.54MPa(950psi)

Journal speed: 0 to 30000 rpm

Dimensionless Parameters

Reynolds Numbers: Rep=467000,Re$_p$=935.0
Speed ParameterΛ: 0 to 0.04783
Rotation Reynolds Number: 0 to 22360

L/D=1, l/L=.354, N·b/πD=.113
c/R=0.002, Hr/c=6

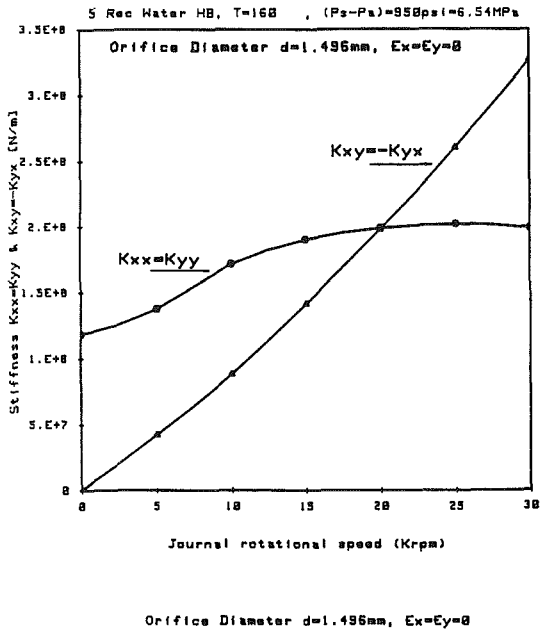

Fig. 8 Predicted stiffness coefficients for test hydrostatic water bearing versus journal rotational speed. Concentric operation, Ps = 6.54 MPa, orifice diameter = 1.496 mm.

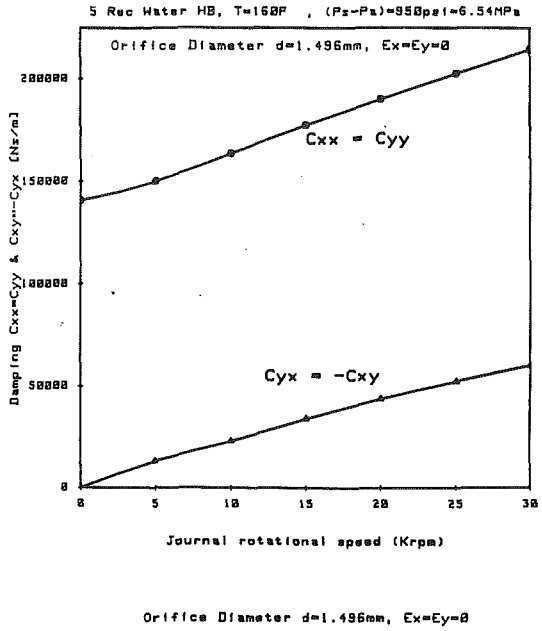

Fig. 9 Predicted damping coefficients for test hydrostatic water bearing versus journal rotational speed. Concentric operation, Ps = 6.54 MPa, orifice diameter = 1.496 mm.

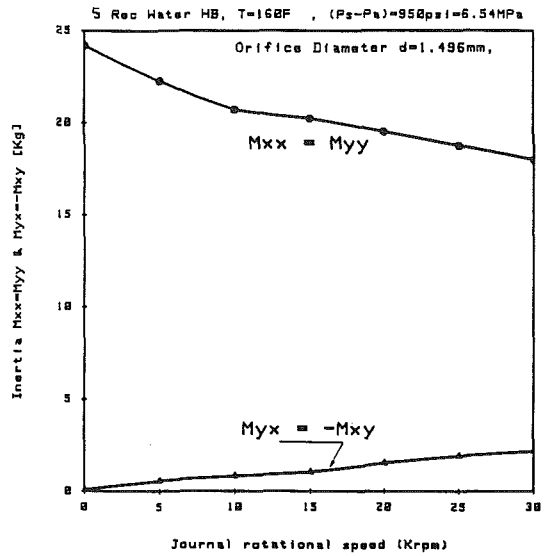

Fig. 10 Predicted inertia force coefficients for test hydrostatic water bearing versus journal rotational speed. Concentric operation, Ps = 6.54 MPa, orifice diameter = 1.496 mm.

consistently higher than the numerical predictions perhaps due to a higher flow resistance at the recesses.

Figure 6 shows pressures measured at the bearing midplane for a load of 760 Newtons at journal speeds equal to 5000 and 8000 rpm. Good correlation between measurements and numerical results is evident. Hydrodynamic effects are dominant in the land between recesses. The measurements show a large edge pressure drop to occur even under an adverse pressure gradient.

Comparisons with the dynamic test data of Murphy and Wagner (1986) have also been performed and found to correlate well. The results are not presented due to space limitations. The present solution offers a considerable improvement over simplified models based on solution to the turbulent Reynolds equation.

A Sample Bearing Problem. A Hydrostatic-Hybrid Bearing Test program is currently under development at Texas A&M University. The objectives of the program are to design and build a test apparatus, systematically test the hydrostatic bearings and, develop an analysis to predict the bearing characteristics and anchor it to the test data.

The hydrostatic bearing test apparatus has been designed and it is currently under construction. Table 2 presents a description of the 5 recess test hydrostatic bearing to be tested initially. The working fluid is hot water and the maximum rated inlet supply fluid pressure is 7.23 MPa (1050 psi). The rotor speed ranges from 0 to 500 Hz (30,000 rpm). For the conditions shown in Table 2, the flow within the bearing is highly turbulent with dominance of hydrodynamic effects at the highest rotational speed. The large value of the modified Reynolds number, Re$_p$*, shows that fluid inertia at film lands has a considerable influence on the bearing static and dynamic force response.

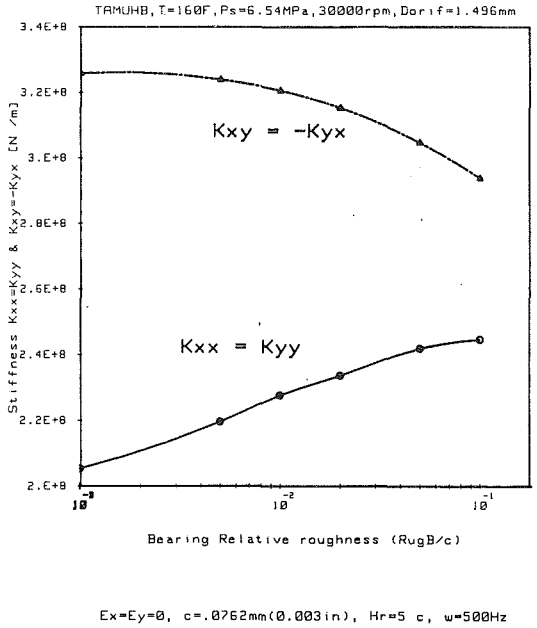

Fig. 11 Predicted stiffness coefficients for test hydrostatic water bearing versus bearing surface relative roughness. Concentric operation, Ps = 6.54 MPa, 30000 rpm, orifice diameter = 1.496 mm.

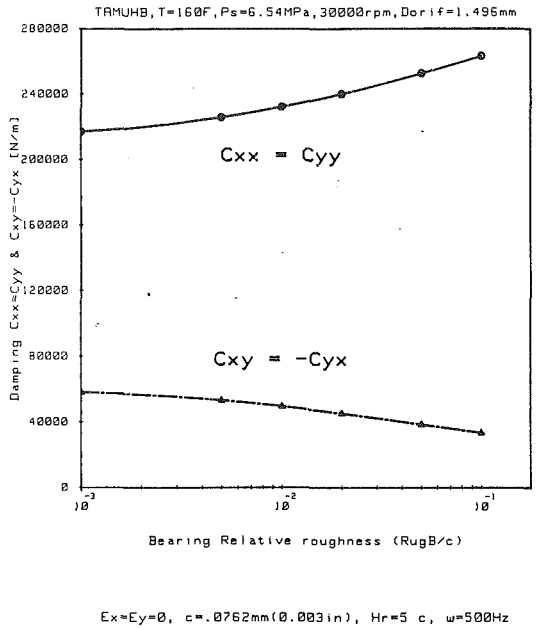

Fig. 12 Predicted damping coefficients for test hydrostatic water bearing versus bearing surface relative roughness. Concentric operation, Ps = 6.54 MPa, 30000 rpm, orifice diameter = 1.496 mm.

The orifices of the test bearing have been sized for a concentric pressure ratio equal to 0.5 at the maximum operating speed of 30,000 rpm. The selected concentric pressure ratio is not necessarily an *optimum* for the present bearing configuration but was chosen on the grounds of common practice for establishing bearing stiffnesses which are not too far from optimum.

Figure 7 shows the predicted bearing flow rate and concentric pressure ratio for increasing journal speeds. The recess pressure ratio increases with speed due to the increased flow resistance caused by the hydrodynamic action, and thus, causes reduced flow rates. Maximum flow rate is attained at zero speed and it is 16 percent higher than for the rated condition at 500 Hz (30,000 rpm). Figures 8 to 10 show the dynamic force coefficients for operation at the centered position. These coefficients have been obtained for excitation frequencies equal to the rotational speed ($\sigma = \Lambda$). The direct stiffnesses increase due to the combined effect of speed and recess pressure. The cross-coupled stiffness and the direct damping coefficient increase very rapidly with speed and, the whirl frequency ratio is equal to 0.50. For pure hydrostatic operation the direct inertia coefficient is a maximum, and then decreases for increasing journal speeds. Cross-coupled damping and inertia coefficients increase linearly with the rotational speed and are mainly due to fluid inertia affecting the bearing hydrodynamic action.

For smooth bearing surface conditions, the predictions show that the stability characteristics of hybrid bearings are not better than for plain journal bearings. These results have brought the need to search for possible remedies to this undesirable condition. A feasible alternative could be the use of a roughened surface HJB. Surface roughness effects are modeled by an effective roughness depth which affects the friction factor formulae based on Moody's equation (Nelson, 1987).

Figures 11 and 12 show the stiffness and damping coefficients versus the bearing surface relative roughness. The roughness parameter varies from 0.1 to 10 percent of the radial clearance. The predictions show that the direct coefficients increase with bearing surface roughness while the cross-coupled stiffness and damping coefficients decrease. The inertia force coefficients (not shown) decrease with increasing bearing surface roughness. The increment in direct stiffness is due to the larger recess pressures attained as the bearing surface roughness increases. The substantial increment in direct damping and reduction in cross-coupled stiffness are a direct consequence of the enhanced bearing surface friction which does not allow the global mean circumferential velocity to be greater than one half the journal surface velocity. Calculations performed show the whirl frequency ratio to drop from a value equal to 0.50 for smooth surfaces to a low value equal to 0.357 for a bearing surface relative roughness equal to 0.1. These results show that the dynamic performance of the hybrid bearing has improved by 27 percent if a roughened bearing surface is used.

Conclusions

The paper has considered the analysis of turbulent flow in hydrostatic/hydrodynamic bearings. Bulk flow equations, including temporal and advective fluid inertia terms, govern the fluid flow in the bearing lands and are coupled to the mass flow constraint at each recess. Flow turbulence is simulated by local friction factors dependent on the Reynolds number and surface condition. At each recess, the mass conservation constraint includes the effect of fluid compressibility. For hybrid operation, the bearing recesses are considered as one-dimensional step bearings, and the local pressure drop at the recess boundary is modeled by Bernoulli equations. The analysis introduces a perturbation method for calculation of the zeroth and first order flow fields determining the bearing steady-state response and dynamic force coefficients, respectively. The nonlinear flow equations are solved numerically by an efficient finite difference method combined with a Newton Raphson technique.

Comparisons of the present full inertial solution with experimental data for turbulent hybrid bearings are regarded as excellent. The present solution shows a considerable improvement over simpler models based on the solution of the turbulent flow Reynolds equations.

Fluid inertia at the film lands is a factor of utmost importance on the static and dynamic performance of hydrostatic and hybrid bearings. Fluid inertia acts as an additional resistance to the flow, and thus, determines higher recess pressures and causes reduced flow rates when compared with predictions not accounting for this effect. In regard to resultant

film forces, fluid inertia at the film lands causes a reduction in the hydrostatic force while increasing substantially the hydrodynamic force. This effect causes a hybrid bearing to operate at higher attitude angles.

The dynamic force coefficients are greatly affected by fluid inertia at the film lands. First, direct stiffness coefficients are found to be lower when compared to an inertialess prediction. This is due to reduced static pressures at the film land regions caused by the increase in dynamic pressure as fluid moves to the bearing exit. Fluid inertia enhances the hydrodynamic and squeeze film actions and causes increased cross-coupled stiffnesses and direct damping coefficients. Inertia force coefficients arise naturally in the full inertial model developed. The magnitude of the direct inertia force coefficients has been determined to be large for bearings with low (c/R) ratios and employing high density fluids. At sufficiently high excitation frequencies, the possibility of net negative dynamic stiffnesses should not be precluded.

The whirl frequency ratio of hybrid bearings at the threshold of instability is equal to 0.50 for concentric operation. Consequently, applications of these type of bearings at speeds well above rotor-bearing system critical speeds may be potentially dangerous. The results also show the convenience of using a deliberately roughened bearing surface to improve the dynamic performance and stability characteristics of high speed hybrid bearings.

Acknowledgments

The generous support of Rocketdyne, the NASA Center for Space Power and the State of Texas Advanced Technology Program is gratefully acknowledged.

References

Artiles, A., Walowit, J, and Shapiro, W., 1982, "Analysis of Hybrid Fluid Film Journal Bearings with Turbulence and Inertial Effects," *Advances in Computer Aided Bearing Design*, ASME Publication G00220, pp. 25–52.

Bou-Said, B., and Chaomleffel, J. P., 1988, "Hybrid Journal Bearings, Theoretical and Experimental Results," ASME Paper 88-Trib-55.

Chaomleffel, J. P., and Nicholas, D., 1986, "Experimental Investigation of Hybrid Journal Bearings," *Tribology International*, Vol. 19, No. 5, pp. 253–259.

Constantinescu, V. N., and Galetuse, S., 1975, "Pressure drop Due to Inertia Forces in Step Bearings," ASME Paper 75-Lub-34.

Deguerce, B., and Nicholas, D., 1975, "Turbulent Externally Pressurized Bearings—Analytical and Experimental Results," Conference on Hybrid Bearings, *Proc. Instn. Mech. Engnrs.*, paper XII(ii), pp. 228–233.

Elrod, H. G., and Ng, C. W., 1967, "A Theory for Turbulent Films and its Application to Bearings," ASME JOURNAL OF LUBRICATION TECHNOLOGY, p. 346.

Ghosh, M. K., Guha, S. K., and Majumdar, B. C., 1989b, "Rotordynamic Coefficients of Multirecess Hybrid Journal Bearings," Part II: Fluid Inertia Effect. *Wear*, Vol. 129, pp. 245–259.

Guidez, J., Juignete, N., and Queval, M., 1981, "Dynamic Behavior of Hybrid Sodium Bearings. Theoretical and Experimental Studies," 6th International Conference on Structural Mechanics in Reactor Technology, Paris, France, August 17–21.

Ho, Y. S., and Chen, N. N., 1980, "Dynamic Characteristics of a Hydrostatic Journal Bearing," *Wear*, Vol. 63, pp. 13–24.

Ho, Y. S., and Chen, N. N., 1984, "Pressure Distribution in a Six-Pocket Hydrostatic Journal Bearing," *Wear*, Vol. 98, pp. 89–100.

Heller, S., 1974, "Static and Dynamic Performance of Externally Pressurized Fluid Film Bearings in the Turbulent Regime," ASME JOURNAL OF LUBRICATION TECHNOLOGY, pp. 381–389.

Hirs, G. G., 1973, "A Bulk Flow Theory for Turbulence in Lubricant Films," ASME JOURNAL OF LUBRICATION TECHNOLOGY, pp. 173–146.

Launder, B. E., and Leschziner, M., 1978, "Flow in Finite-Width, Thrust Bearings Including Inertial Effects, I—Laminar Flow, II- Turbulent Flow," ASME JOURNAL OF LUBRICATION TECHNOLOGY, Vol. 100, pp. 330–345.

Lingard, S., Chen, N. N., and Kong, Y. C., 1982, "Aspects of the Performance of Externally Pressurized Journal Bearings," *Wear*, Vol. 78, pp. 343–353.

Murphy, B. T., and Wagner, M. N., 1986, "Measurement of Rotordynamic Coefficients for a Hydrostatic Radial Bearing," Advanced Earth-to-Orbit Propulsion Technology Conference, Huntsville, AL.

Nelson, C. C., and Nguyen, D. T., 1987, "Comparison of Hir's Equation with Moody's Equation for Determining Rotordynamic Coefficients of Annular Pressure Seals," ASME JOURNAL OF LUBRICATION TECHNOLOGY, Vol. 109, pp. 144–148.

Redecliff, J. M., and Vohr, J. H., 1969, "Hydrostatic Bearings for Cryogenic Rocket Engine Pumps," ASME JOURNAL OF LUBRICATION TECHNOLOGY, pp. 557–575.

Van Doormaal, J. P., and Raithby, G. D., 1984, "Enhancements of the SIMPLE Method for Predicting Incompressible Fluid Flows," *Numerical Heat Transfer*, Vol. 7, pp. 147–163.

APPENDIX A

The perturbed shear coefficients for the first-order solution are given by:

$$\gamma_{uu} = \frac{k_{x0}}{h_0} + f_{J1}(u_0 - \Lambda)^2 + f_{B1}u_0^2 \tag{A.1}$$

$$\gamma_{vv} = \frac{k_{y0}}{h_0} + (f_{J1} + f_{B1})v_0^2 \tag{A.2}$$

$$\gamma_{vu} = \gamma_{uv} = f_{J1}(u_0 - \Lambda)v_0 + f_{B1}u_0v_0 \tag{A.3}$$

$$\gamma_{u0} = \frac{u_0}{h_0^2}[-K_{x0} + C_{CJ} + C_{CB}] - \frac{\Lambda}{h_0^2}[C_{CJ} - K_xK_{J0}/2] \tag{A.4}$$

$$\gamma_{v0} = \frac{v_0}{h_0^2}[-K_{y0} + C_{CJ} + C_{CB}] \tag{A.5}$$

where:

$$C_{CJ} = (1/2)[R_JC_J + 5\times 10^5]\gamma_J$$
$$C_{CB} = (1/2)[R_BC_B + 5\times 10^5]\gamma_B \tag{A.6}$$

$$f_{J1} = \frac{\mathrm{Re}_p^2 h_0}{2R_J}[f_{J0} + \beta_J\gamma_J];$$
$$f_{B1} = \frac{\mathrm{Re}_p^2 h_0}{2R_B}[f_{B0} + \beta_B\gamma_B] \tag{A.7}$$

$$\gamma_J = \frac{-0.001375/2.65}{[f_{J0}/0.001375 - 1]^{1.65}}; \tag{A.8}$$

$$\gamma_B = \frac{-0.001375/2.65}{[f_{B0}/.001375 - 1]^{1.65}}$$

$$\beta_J = 5\times 10^5/R_J;$$
$$\beta_B = 5\times 10^5/R_B \tag{A.9}$$

$$C_J = 10^4\frac{r_J}{Ch_0};$$
$$C_B = 10^4\frac{r_B}{Ch_0} \tag{A.10}$$

and

$$R_J = \mathrm{Re}_p h_0[(u_0 - \Lambda)^2 + v_0^2]^{1/2}$$
$$R_B = \mathrm{Re}_p h_0[(u_0^2 + v_0^2]^{1/2} \tag{A.11}$$

are the Reynolds numbers relative to the journal and bearing surfaces, respectively.

For laminar flows,

$$\gamma_{uu} = \gamma_{vv} = 12/h_0,\ \gamma_{uv} = \gamma_{vu} = 0$$
$$\text{and } \gamma_{v0} = -2\times 12\ v_0/h_0^2,\ \gamma_{u0} = (-2\times 12\ u_0 + 12\Lambda)/h_0^2 \tag{A.12}$$